Modeling Black Hole Frequency Spectra with Non-Standard Accretion Disk Models

Chau Truong

Department of Physics, Princeton University

Advisor: Frans Pretorius, Delilah Gates

Abstract

X-ray reflection spectroscopy is a technique commonly used to measure the spin of a black hole (BH). The method involves simulating and observing the Fe-Kα line emission from a BH accretion disk, which is broadened into a spectrum by the effects of relativistic Doppler shift and gravitational redshift. The resulting shape of the broadened emission line encodes crucial information about the BH spin. Previous applications of this method have predominantly employed a standard accretion disk model in which the disk particles travel on stable circular, i.e. Keplerian, orbits. This study aims to explore the effects of deviating from this standard disk model on the emission line spectrum, with a specific focus on the model of sub-Keplerian flow. In this model, disk particles travel on circular orbits with their angular momentum rescaled by a sub-Keplerianity parameter ξ compared to that of the standard model. Our approach involves using the adaptive analytical ray tracing code `AART` to simulate high-resolution images of BH accretion disks, calculating the disk radius from which observed photons were emitted r and redshift factor g of the photons at each pixel on the image. This paper presents simulated emission line spectra for various sub-Keplerianity parameter values, considering different spin and observer inclination cases. Despite some limitations, our work lays a foundational framework for future simulations of iron line spectra using non-standard accretion disk models.

This paper represents my own work in accordance with University regulations.

/s/ Chau Truong

1 Introduction

Einstein's theory of general relativity predicted the existence of black holes (BHs), massive objects defined by their event horizon, the radial distance from the BH center at which the escape velocity is equal to the speed of light. Consequently, stationary (non-moving) BHs must be studied by examining the electromagnetic radiation emitted by sources orbiting around them, and BHs in binary systems can be studied through their emitted gravitational waves, ripples in spacetime caused by highly accelerated masses.

Astrophysical BHs are characterized by two properties: their mass M and their angular momentum $J = aGM/c$, where a is the spin parameter with units of mass, G is Newton's gravitational constant, and c is the speed of light. It is common to work in "natural units," where $G = c = 1$, leaving $J = aM$. To convert quantities from natural units back to real units, we can perform dimensional analysis and multiply the quantities by factors of G and c.

The particles traveling around a BH make up what is called the accretion disk. The mass of a BH can be found by measuring the motion of objects orbiting around it. The motion of stars has been used measure the masses of M87* [1], the BH at the center of the elliptical galaxy Messier 87, and SgrA* [2], the BH at the center of our very own galaxy, the Milky Way. For objects orbiting closer to the BH event horizon, general relativistic effects must be taken into account. However, we can illustrate how to perform the mass calculation using Newtonian gravity. For objects sufficiently far from the BH, we can measure the BH mass by applying Newton's law of universal gravitation:

$$F_g = \frac{GMm}{r^2}. \tag{1}$$

Assuming that the objects are traveling in circular orbits, the gravitational force can be set equal to the centripetal force:

$$\frac{GMm}{r^2} = \frac{mv^2}{r}, \tag{2}$$

where M is the mass of the BH, m is the mass of an object traveling around it, v is the object's velocity, and r is the radial distance from the object to the BH. Performing a simple calculation, we obtain

$$M = \frac{v^2 r}{G}. \tag{3}$$

For objects located closer to the BH event horizon, general relativistic effects cannot be ignored. In such case, the BH mass can be measured through the effects of the gravitational lensing of light around it, which occurs when a massive celestial object, such as a BH or a galaxy, causes a significant curvature of spacetime such that the path of light around the object is bent. Light that orbits around the BH multiple times becomes concentrated into a bright ring in a BH image, with a radius roughly proportional to the mass of the BH. The Event Horizon Telescope has measured the masses of M87* [3] and SgrA* [4] using this method.

Measuring the spin of a BH poses a significant challenge. One method of doing so uses the X-ray reflection method, described by George and Fabian in [5]. This technique involves modeling the broadened frequency spectrum of a single frequency emission, with the resulting

shape of the line profile containing information about the BH spin. To date, over 20 BH spin measurements have been made using this method. Recently, a proposal was made for the Advanced Telescope for High-Energy Astrophysics (Athena) observatory mission, which aims to use an imaging spectrometer called the X-ray Integral Field Unit (X-IFU) to provide spatially resolved high-resolution X-ray spectroscopy. Past measurements using the X-ray reflection method have relied on the assumption that the accretion disk particles are moving in the equatorial plane on stable circular orbits [6] [7]. However, this model neglects any interactions the disk may have with itself, such as the disk particles colliding into each other, potentially causing real accretion disks to deviate from the model.

The goal of this paper is to determine how deviations from the standard disk model of a stable circular orbit affect the shape of the frequency emission spectra. Throughout this paper, we will discuss the X-ray reflection method and the characteristics of the resulting broadened frequency spectrum (Section 2). Our discussion will continue with an explanation of how we proceeded to simulate the frequency spectra (Section 3) and how we produced code to simulate spectra for non-standard models (Section 4). Finally, we will analyze the trends observable from the spectra we created and compare them to those of the standard disk model (Section 5).

2   The X-ray Reflection Method

The X-ray reflection method has allowed for over 20 measurements of BH spin [6] [7]. In this section, we will briefly describe the method and discuss the characteristics of the resulting broadened emission line.
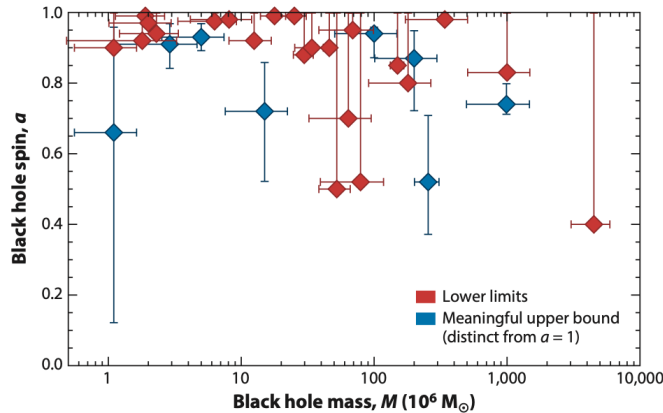

Figure 1: Supermassive BH spins as a function of mass from Reynolds [8].

The X-ray reflection method uses atomic spectroscopy to measure BH spin. When an atom absorbs electromagnetic radiation, it becomes excited, causing at least one of its electrons to jump to a higher energy level. However, the electrons do not stay in the excited state for long and eventually return to their ground states. When they do, the atom will, in turn, emit radiation at specific frequencies.

Many active galactic nuclei (AGN), galactic centers where supermassive BHs are housed, and accreting stellar-mass BHs in X-ray binaries possess a hot corona of electron-positron plasma ($T \sim 10^9$ K) above the accretion disk that produces hard X-rays. These X-ray emissions irradiate the cold gas of the accretion disk, causing the surface layers of the disk to become excited and emit fluorescent emission lines at distinct X-ray frequencies. Due to the high astrophysical abundance and fluorescent yield of iron, the most prominent emission line is the Fe-Kα line that has a rest frame energy of 6.4 keV [5]. This emission line is broadened due to the effects of relativistic Doppler shift and gravitational redshift, both of which are described below.

2.1   Relativistic Doppler Shift

The Doppler shift is the change in frequency caused by the relative motion of the source of the emission and that of the observer.

In the simple case where both the source and the observer are stationary, we have the frequency of the source $\nu = 1/T$, where T is the period, and the corresponding wavelength $\lambda = \nu T = c/\nu$, where c is the speed of light.

When the source is moving towards the observer with a constant speed v, the light seen by the observer will have a shorter wavelength than it had when it was originally emitted. The Doppler-shifted wavelength of the emissions is

$$\lambda' = \lambda - vT. \tag{4}$$

Using the relationship between the wavelength and frequency $\lambda' = c/\nu'$, we find

$$g_{Dopp} = \frac{\nu'}{\nu} = \frac{1}{1 - v/c}, \tag{5}$$

where g_{Dopp} is the Doppler shift factor, and can conclude that light emitted from a source moving towards an observer will have a higher frequency than it would have if the source was at rest. In this case, g_{Dopp} would be the Doppler blueshift factor.

Similarly, in the case where the source is moving away from the observer with a constant speed v, the observer will see light with a wavelength longer than the emitted wavelength, with frequency

$$g_{Dopp} = \frac{\nu'}{\nu} = \frac{1}{1 + v/c}. \tag{6}$$

Thus, light emitted from a source moving away from an observer will have a lower frequency than it would have if the source was at rest. Here, g_{Dopp} is the Doppler redshift factor.

These equations for the Doppler shift factors can be rewritten to take into account the effects of time dilation. As stated by Einstein's theory of special relativity, the frequency of light emissions is slowed down by a factor of

$$\gamma = \frac{1}{\sqrt{1 - (v/c)^2}}. \tag{7}$$

The Doppler shift factor now becomes

$$g_{Dopp} = \frac{\nu'}{\nu} = \sqrt{\frac{1 + v/c}{1 - v/c}}, \tag{8}$$

where v is the speed of the source as it travels in the direction of the observer (positive v) or away from the observer (negative v).

2.2 Gravitational Redshift

Gravitational redshift is the frequency shift caused by the motion of a photon traveling away from a massive body.

We imagine the gravitational potential caused by a massive object as a basin, similar to a trampoline with a bowling ball resting in the center of it, and the motion of particles and other celestial objects traveling around the massive body to be analogous to marbles traveling along the surface of the basin. A particle traveling away from the center of a massive object, away from the basin or gravitational well, must expend energy in order to escape the object's gravitational field and will therefore lose energy. For photons, which must always travel at the speed of light, a decrease in energy will manifest as a decrease in frequency. The frequency decrease will correlate to an increase in the wavelength of the photon, causing a gravitational redshift. By contrast, a photon traveling towards the center of a massive object, into the gravitational well, will undergo an increase in energy and frequency. The increase in frequency will result in a decrease in the wavelength of the photon, causing a gravitational blueshift. An observer located far away will only receive light that is gravitational redshifted because the photons are traveling towards the observer and away from the massive object.

Here, we will derive the gravitational redshift factor in the Newtonian case. The potential energy of a particle traveling under the influence of the gravitational force exerted by a massive object is given by $PE = -GMm/r$, where M is the mass of the massive central object, m is the mass of the particle, and r is the radial distance from the particle to the center of the massive object. The kinetic energy of a photon is given by $E = h\nu$. Relating this to the mass-energy relation $E = mc^2$, where c is the speed of light, the "inertial mass" of a photon is found to be

$$m = \frac{h\nu}{c^2}.$$
(9)

The total energy of a photon under the influence of gravity is given as

$$E' = h\nu - \frac{GMm}{r} = h\nu - \frac{GM}{r}\frac{h\nu}{c^2},$$
(10)

where $E' = h\nu'$. Solving for the gravitational redshift factor,

$$g_{grav} = \frac{\nu'}{\nu} = (1 - \frac{GM}{rc^2}).$$
(11)

In our following work, we will combine the effects of these two sources of frequency shifting and relativity to discuss the frequency of light near a BH as seen by an observer far away. We will work in terms of a total "g-factor" or "redshift factor" g, where

$$g = \frac{E_{observed}}{E_{emitted}}.$$
(12)

2.3   Broadened Iron Emission Line

The broadened Fe-Kα iron emission line resulting from the relativistic Doppler shift and gravitational redshift is characterized by a sharp blueshifted peak and a long redshifted tail, shown in Figure 2. The maximum flux of the blueshifted peak and the energy at which the redshifted tail truncates are linked to the spin of the BH [9]. According to the standard disk model of circular Keplerian flow first used by Cunningham, the disk particles travel on circular orbits until they reach the innermost stable circular orbit (ISCO) and spiral inwards towards the event horizon while conserving the energy, angular momentum, and Carter constant of particles orbiting at the ISCO radius [10]. Often, the ISCO is taken to be the inner edge of the accretion disk. In such case, as the BH spin increases and the location of the ISCO moves closer to the event horizon, the gravitational redshift of X-rays reflected from the innermost part of the disk becomes progressively larger and the redshifted tail in spectrum lengthens [6]. At radii closest to the horizon, where matter travels at relativistic speed, the blueshift on the particles on the approaching side of the accretion disk can be large, surpassing the gravitational redshift and resulting in an observed net blueshift. The blueshifted part of the broadened iron line retains a finite flux up to a sharp peak, corresponding to the maximum observable blueshift (MOB) [9].

Code that have been written to create iron line spectra include `xillver` [11] [12], `relline` [13] [14], and `relxill` [15] [16].
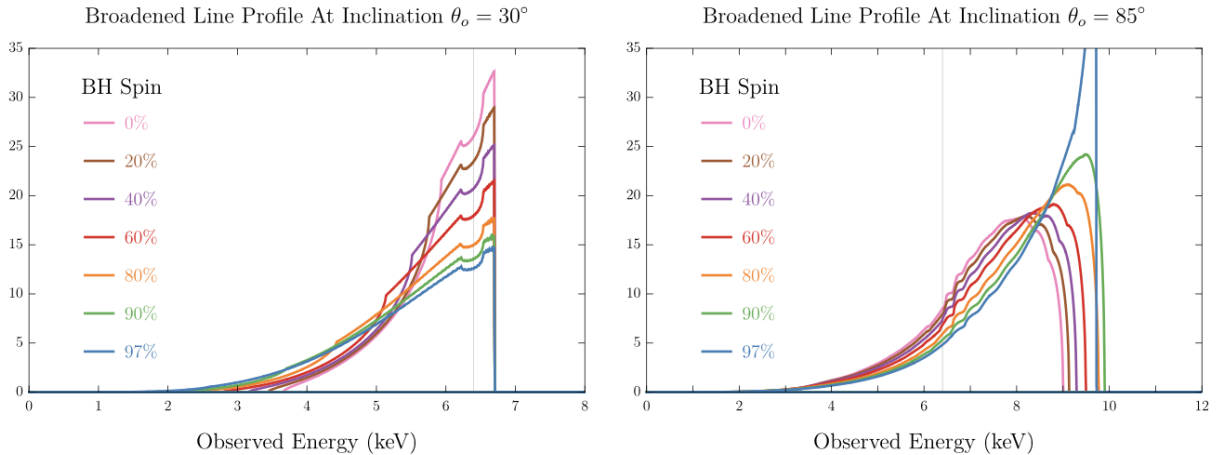

Figure 2: Specific flux density as a function of observed photon energy as a result of relativistic broadening of the Fe-Kα iron emission line from Gates [9], simulated using numerical code `relline` [13]. Features worth noting include the blueshifted peak (to the right) and the redshifted tail (to the left).

3   Creating Simulations of Iron Emission Line Spectra

Measurements of BH spin are performed by comparing known data from observed X-ray emissions to simulated iron line spectra. To simulate an iron emission line spectrum, an

image of the accretion disk around a BH must be simulated first. From the description of the motion of the orbiters in the disk and how emissive, or bright, the material is, we can integrate over the image, collecting the photons at each pixel and binning them by their observed energy. For the purposes of this paper, we are using the Novikov-Thorne model of a geometrically thin, optically thick accretion disk [17]. We are also assuming the accretion disk is in the equatorial plane with $\theta = \pi/2$, where θ is the angle with respect to the spin axis from which the observer is viewing the BH.

3.1 Motion of Particles Around a BH

To describe a point in curved spacetime in general relativity, the Boyer-Lindquist coordinate system is used, with unit directions $\hat{t}$, $\hat{r}$, $\hat{\theta}$, $\hat{\phi}$ [18]. We use the following matrix, dubbed the "metric", to define the inner product of vectors in spacetime:

$$g_{\mu\nu} = \begin{bmatrix} -1 + \frac{2Mr}{\Sigma} & 0 & 0 & -\frac{2Mar}{\Sigma}\sin^2\theta \\ 0 & \frac{\Sigma}{\Delta} & 0 & 0 \\ 0 & 0 & \Sigma & 0 \\ -\frac{2Mar}{\Sigma}\sin^2\theta & 0 & 0 & -\frac{(r^2+a^2)^2 - a\Delta\sin^2\theta}{\Sigma}\sin^2\theta \end{bmatrix}, \tag{13}$$

where

$$\Delta = r^2 - 2Mr + a^2, \qquad \Sigma = r^2 + a^2\cos^2\theta. \tag{14}$$

The root of Δ define the event horizon of the BH

$$r_H = M + \sqrt{M^2 - a^2}. \tag{15}$$

Given two vectors in spacetime $v = \begin{bmatrix} v^t & v^r & v^\theta & v^\phi \end{bmatrix}$ and $w = \begin{bmatrix} w^t & w^r & w^\theta & w^\phi \end{bmatrix}$, the metric allows us to take their inner product:

$$v \cdot w = \begin{bmatrix} v^t & v^r & v^\theta & v^\phi \end{bmatrix} \begin{bmatrix} -1 + \frac{2Mr}{\Sigma} & 0 & 0 & -\frac{2Mar}{\Sigma}\sin^2\theta \\ 0 & \frac{\Sigma}{\Delta} & 0 & 0 \\ 0 & 0 & \Sigma & 0 \\ -\frac{2Mar}{\Sigma}\sin^2\theta & 0 & 0 & -\frac{(r^2+a^2)^2 - a\Delta\sin^2\theta}{\Sigma}\sin^2\theta \end{bmatrix} \begin{bmatrix} w^t \\ w^r \\ w^\theta \\ w^\phi \end{bmatrix}. \tag{16}$$

The non-diagonality of $g_{\mu\nu}$ is related to the property that spacetime is not flat. However, when $g_{\mu\nu}$ is evaluated for $r \to \infty$, we recover the metric for flat spacetime in the case of special relativity in spherical coordinates:

$$\lim_{r \to \infty} g_{\mu\nu} = \begin{bmatrix} -1 & 0 & 0 & 0 \\ 0 & 1 & 0 & 0 \\ 0 & 0 & r^2 & 0 \\ 0 & 0 & 0 & r^2\sin^2\theta \end{bmatrix}. \tag{17}$$

The motion of a particle of mass m around a BH can be described by its four-momentum

$$p = \begin{bmatrix} p^t & p^r & p^\theta & p^\phi \end{bmatrix}, \tag{18}$$

7

where $p \cdot p = -m^2$. The angular velocity Ω of the particle (relative the BH's spin axis) is given by

$$\Omega = \frac{u^\phi}{u^t}. \tag{19}$$

The motion of particles moving along the curvature of spacetime without the influence of external forces, such as collisions or interactions with other particles, are said to be geodesic. For these particles, the energy and angular momentum are conserved. The energy E is first component of the vector $-g_{\mu\nu}p$:

$$E = \left(1 - \frac{2Mr}{\Sigma}\right) p^t + \left(\frac{2Mar}{\Sigma} \sin^2 \theta\right) p^\phi. \tag{20}$$

The angular momentum L is the fourth component of the vector $g_{\mu\nu}p$:

$$L = \left(-\frac{2Mar}{\Sigma} \sin^2 \theta\right) p^t + \left(-\frac{(r^2 + a^2)^2 - a\Delta \sin^2 \theta}{\Sigma} \sin^2 \theta\right) p^\phi. \tag{21}$$

It is worth noting that particle with zero angular momentum ($L = 0$) still has a positive angular velocity ($\Omega > 0$) when the BH is spinning ($a > 0$). This phenomenon is called "frame dragging," when the BH drags spacetime around it.

3.2 BH Images

Due to the extreme lensing behavior of BHs, there are infinitely many paths light can take from a source point on the equatorial plane of the accretion disk to the observer, with each path orbiting around the BH a different number of times. Consequently, images of a BH surrounded by an optically thin accretion disk can be decomposed into multiple layers, each labeled by a half-orbit number n, representing the number of times the light rays from the source crosses the equatorial plane [19] [20]. Each layer is a full lensed image of the main accretion disk emission, with the direct image ($n = 0$) displaying a central dark area, the BH, encircled by the primary image of the accretion flow into the hole [19]. The nth lensing band is defined as the exponentially small (in n) layer of the image consisting only of the light rays that cross the equatorial plane n times.

Images of BHs can be simulated through ray tracing, a method of generating digital images by simulating and tracing the path that light rays would take from a source, the BH accretion disk, to the observer. In backwards ray tracing, the paths are instead traced from the observer back to the source.

For each pixel in the simulated image, we can analytically calculate the four-momentum of the particles, or the photons, that arrive to the observer from that point on the image screen as a function of the screen coordinates x and y, along with the half-orbit number n. The momentum of a photon is proportional to the observed energy: $p(x, y, n) = E_o f(x, y, n)$. We can also analytically calculate the radial distance from the BH center in the equatorial plane that each photon arrives from, the disk radius, r as a function of the same variables: $r(x, y, n)$.

Once again, we are assuming the Novikov-Thorne model of a geometrically thin, optically thick accretion disk. Thus, any light ray crossing the equatorial plane is absorbed, and we will only simulate direct BH images of the $n = 0$ lensing band.
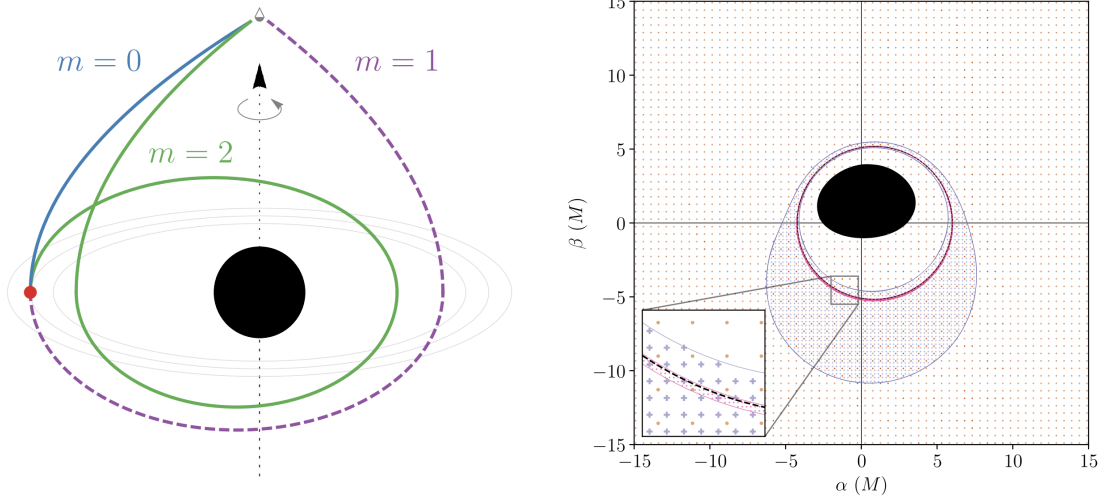
Figure 3: Illustration of a light ray from an equatorial emission source crossing the equatorial plane $n = m$ times for each lensing band from [20] (left). Illustration of lensing bands with different grid resolutions from `AART` [19], with the orange, purple, magenta marks representing light rays from the $n = 0, 1, 2$ lensing bands, respectively (right).

3.3   Calculating Redshift Factor

If we are provided with information about the motion of the particles in the BH accretion disk, we are able to calculate the redshift factor of the emission from the particles.

Massive particles can be described by a four-velocity

$$u = \frac{p}{m} = \begin{bmatrix} u^t & u^r & u^\theta & u^\phi \end{bmatrix}. \tag{22}$$

Since we are only considering motion fixed in the equatorial plane of the accretion disk with $\theta = \pi/2$, we set $u^\theta = 0$. This leaves the four-velocity as

$$u = \begin{bmatrix} u^t & u^r & 0 & u^\phi \end{bmatrix}. \tag{23}$$

The redshift factor is given by Cárdenas-Avendaño et al. in [19] as

$$g = -\frac{E_o}{p \cdot u}, \tag{24}$$

where E_o is the observed energy of the photon, p is the four-momentum of the photon, and u is the four-velocity of the disk particle that emitted the photon. The four-momentum p can be rewritten in terms of a vector f that is rescaled by the observed energy E_o:

$$p = \begin{bmatrix} p^t & p^r & p^\theta & p^\phi \end{bmatrix} \tag{25}$$
$$= E_o \begin{bmatrix} f^t & f^r & f^\theta & f^\phi \end{bmatrix} \tag{26}$$
$$= E_o f \tag{27}$$

9

Consequently, the redshift factor can also be rewritten in terms of f:

$$g = -\frac{E_o}{p \cdot u} = -\frac{E_o}{E_o(f \cdot u)} = -\frac{1}{f \cdot u}. \tag{28}$$

The first image of a BH accretion disk of particles traveling on circular orbits simulated using backwards ray tracing to calculate the disk radius and redshift factor of photons from each pixel was simulated by Luminet in 1979 [21]. The images he simulated were of disks around non-spinning BHs ($a = 0$).

3.4 Building a Spectrum From a Simulated Image

After simulating an image of a BH accretion disk from a given disk model described by parameters such as the spin a and the inclination angle at which the observer is viewing the BH θ, we are able to compute the iron line profile.

Given a simulated image, we first count the number of photons and measure the redshift factor g of their emission for each pixel on the image screen. For each g, the corresponding observed energy in keV can be calculated with $E_o = gE_e$, where E_o is the observed energy and E_e is the emitted energy. Here, $E_e = 6.4$ keV, the rest frame energy of the Fe-Kα emission line. With the number of photons and observed energy calculated at each pixel, a histogram can be plotted where the bins are categorized by specified intervals of the observed energy and the height of the bins represent the number of photons counted for each energy interval.

Following Cunningham [10], we compute the iron line profile using the transfer function

$$F(g) = \int g^3 I_e(r) \, dx \, dy, \tag{29}$$

where x and y represent the different directions on the image screen. We also specify the emissivity with $I_e(r) = r^{-3}$ for the $n = 0$ band, representing how much light is emitted by a particle at a disk radius r. We take $I_e(r) = 0$ for all other bands $n > 0$, as we are assuming the disk to be optically thick. To calculate the line profile given a simulated image, we must discretize the above function:

$$F(E_o) = \sum_{i,j} = g_{ij}{}^3 \, r_{ij}{}^{-3} \, dx \, dy, \tag{30}$$

where i corresponds to the x coordinates of the image screen, j corresponds to the y coordinates, and dx and dy represent the length and height of each pixel.

Given the discretized transfer function for the broadened iron line, we adjust the weight of the height of the bins of the histogram accordingly to display the observed accretion disk flux for each energy interval instead. Finally, we are able plot a curve, where the x-coordinates of the points along the curve are the midpoints of each bin and the corresponding y-coordinates of the points are the heights of each bin. The curve obtained is the broadened iron emission line desired.
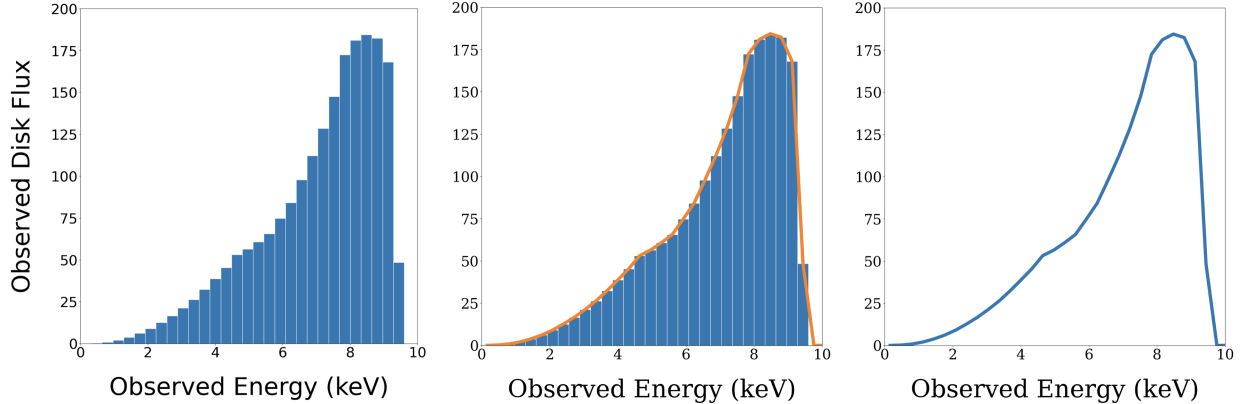
Figure 4: The sequences of steps required to construct a broadened iron emission line given a disk model simulated using code `AART` [19]: histogram of photon flux for each observed energy (left), curve superimposed above histogram with bin midpoints and bin heights as x and y coordinates respectively (center), final iron line (right). For this spectrum, spin $a = 0.7$, observer inclination $\theta = 70°$, and bin width $dE = 0.05$ were used.

4 Code for Spectra

The code used in this paper to simulate the high-resolution images of BH accretion disks is `AART`, an adaptive analytical ray tracing code courtesy of Alejandro Cárdenas-Avendaño, Alexandru Lupsasca, and Hengrui Zhu [19] [22].

4.1 `AART`

`AART` computes the lensing bands for a given BH spin a and observer inclination θ and uses backwards ray tracing to create BH images [19]. `AART` implements the backwards ray tracing analytically, allowing the user to choose different image screen resolutions for each lensing band calculation.

Beginning with the $n = 0$ lensing band, `AART` creates a Cartesian grid that covers the desired area of the image and ray traces the image of the equatorial emission source layer by layer. For each subsequent layer, `AART` uses a grid with a resolution chosen by the user and only ray traces pixels contained in the lensing band that make up the layer. In doing so, `AART` is able to generate BH images with improved efficiency [19]. The right panel in Figure 3 depicts light rays from the $n = 0$, 1, 2 lensing bands at different grid resolutions calculated in `AART`.

`AART` is designed to export the disk radius r and redshift factors g of particles in the disk for each pixel in the images it simulates for various disk models. These quantities will serve as input for this study.
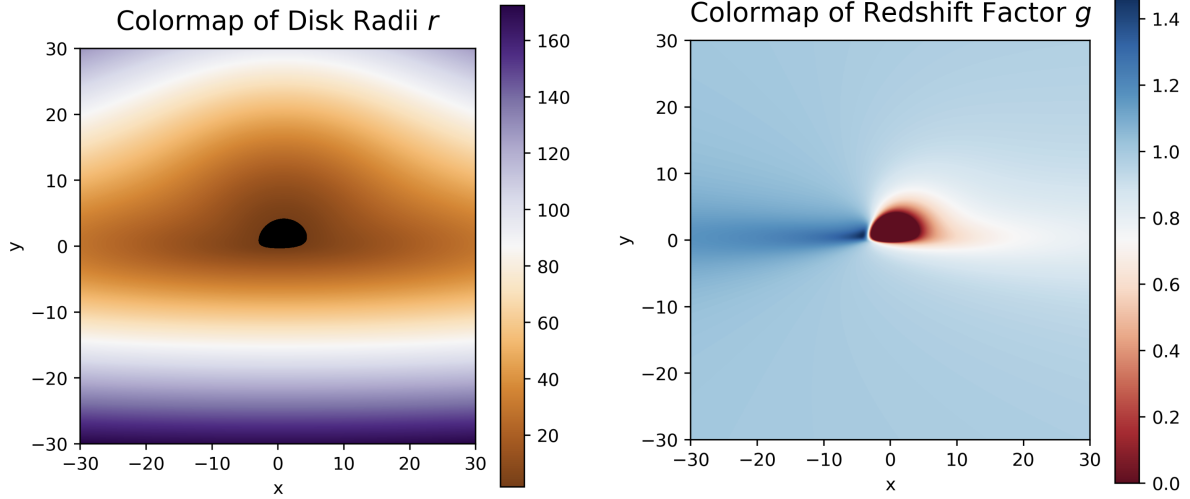
Figure 5: Colormaps depicting the disk radius r (left) and the redshift factor g (right) of photons in each pixel of the BH image, calculated using `AART` [22]. Simulated using $a = 0.7$ and $\theta = 70°$.

4.2 `AART` Disk Models

Accretion disk flow is typically separated into two regions. In the first region, or the "outer" disk, we consider particles traveling at a radius $r \geq r_{ISCO}$. In the second region, or the "inner" disk, we consider particles traveling at a radius $r < r_{ISCO}$. The ISCO radius is evaluated by Bardeen et al. in [23]:

$$r_{ISCO} = M[3 + Z_2 - \sqrt{(3 - Z_1)(3 + Z_1 + 2Z_2)}] \tag{31}$$

$$Z_1 = 1 + \sqrt[3]{1 - (a/M)^2}[\sqrt[3]{1 + a/M} + \sqrt[3]{1 - a/M}] \tag{32}$$

$$Z_2 = \sqrt{3(a/M)^2 + Z_1^2} \tag{33}$$

where r_{ISCO} is a function of the BH's mass and spin. When the BH is non-rotating ($a = 0$), $r_{ISCO} = 6M$. When it is maximally rotating and $a = M$, $r_{ISCO} = M$.

`AART` allows the user to set the BH spin a, the inclination angle from the spin axis of the BH at which we are observing it θ, the image resolution in each lensing band, and specific values for the disk parameters. The disk parameters include the sub-Keplerianity factor ξ, and superposition control parameters β_r and β_ϕ, which describe a generalized accretion flow that interpolates between sub-Keplerian orbits and radial infall. The specific values chosen for the parameters determine the disk model that is to be used, and from there, `AART` is able to simulate an image of the accretion disk and compute the disk radii r and redshift factors g.

The following disk models are programmed into `AART` using natural units $G = c = 1$, which includes the standard disk model of a stable circular orbit, along with the non-standard models of pure radial infall, sub-Keplerian flow, and a combination of the two.

4.2.1 Standard Model of Circular Keplerian Flow

In the standard model used for modeling broadened iron lines, first used by Cunningham in [10], all particles in the accretion disk traveling outside the ISCO radius move on stable circular equatorial geodesic orbits. Particles traveling inside the ISCO radius move on unstable inspiraling geodesic orbits, falling into the event horizon, while conserving the energy, angular momentum, and Carter constant of particles orbiting at the ISCO radius. The four-velocity of particles in the standard model is denoted as $u = \mathring{u}$ [19].

4.2.2 Pure Radial Infall

The four-velocity of radially infalling particles traveling in geodesic motion is denoted as $u = \bar{u}$ [19]. These particles have zero initial velocity at infinity and conserved angular momentum and obtain radial and angular velocities as they fall in.

4.2.3 Sub-Keplerian Flow

Let $u = \hat{u}$ be the four-velocity of particles traveling in non-geodesic sub-Keplerian motion [19]. In this model, the angular momentum of the geodesic, circular Keplerian flow L is rescaled by a sub-Keplerianity parameter ξ, where $0 < \xi \leq 1$:

$$\hat{L} = \xi \mathring{L}. \tag{34}$$

When $\xi = 1$, we recover the standard model of circular Keplerian flow. In this paper, we will investigate the effects of altering ξ on the broadened iron emission line produced by the X-ray reflection method.

4.2.4 Combining Motions

To interpolate between the previous two models, pure radial infall and sub-Keplerian flow, we follow Vincent et al. [24] and Pu et al. [25] and introduce

$$\tilde{u}^r = \hat{u}^r + (1 - \beta_r)(\bar{u}^r - \hat{u}^r) \tag{35}$$

$$\tilde{\Omega} = \hat{\Omega} + (1 - \beta_\phi)(\bar{\Omega} - \hat{\Omega}) \tag{36}$$

where $0 \leq \beta_r \leq 1$ controls the radial components of the linear superposition and $0 \leq \beta_\phi \leq 1$ controls the angular components [19]. When $\beta_r = \beta_\phi = 0$, we recover the pure radial infall model, $\tilde{u}^r = \bar{u}^r$ and $\tilde{\Omega} = \bar{\Omega}$. When $\beta_r = \beta_\phi = 1$, we recover the model of sub-Keplerian flow, $\tilde{u}^r = \hat{u}^r$ and $\tilde{\Omega} = \hat{\Omega}$.

4.3 Modified-`AART`

With the disk radii r and redshift factors g calculated in `AART` for a given BH spin and inclination, we implemented the method described in Section 3.4 and wrote a function to plot the broadened iron emission line, shown in Figure 4.

To decrease the runtime when computing the broadened emission spectrum, we altered `AART` to create a polar grid rather than a Cartesian grid when calculating the lensing bands.

This way, the program will ray trace more pixels closer to the BH, where relativistic effects are stronger, and less pixels farther from the BH. When computing the iron line profile, we must perform a change of variables on the transfer function defined by Cunningham in [10] to convert from Cartesian to polar coordinates of the image screen:

$$F(g) = \int g^3 I_e(r) \, \rho \, d\rho \, d\varphi, \tag{37}$$

where we used the Jacobian $J(\rho, \varphi) = \rho$. Here, ρ represents the radial direction on the image screen, and φ represents the angular direction. The discretized form of the function is as follows:

$$F(E_o) = \sum_{i,j} = g_{ij}{}^3 \, r_{ij}{}^{-3} \, \rho_{ij} \, d\rho \, d\varphi, \tag{38}$$

where i corresponds to the ρ coordinates of the image screen, j corresponds to the φ coordinates, and $d\rho$ and $d\varphi$ represent the radial and angular size of each pixel.

Additionally, since we are under the assumption that the accretion disk is optically thick and that any light ray crossing the equatorial plane will be absorbed by the disk, we altered AART to only calculate the $n = 0$ lensing band, further reducing runtime.
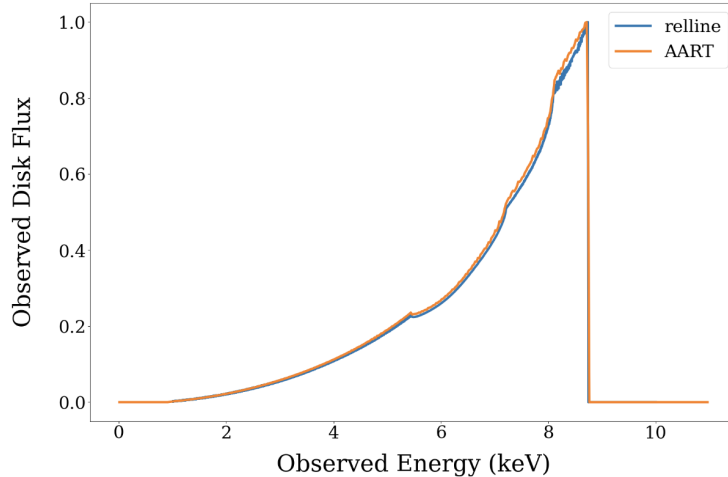

Figure 6: The broadened iron emission line for spin $a = 94\%$, inclination angle $\theta = 75°$, and outer disk edge $r = 50M$ constructed with code from relline [13] and AART [19], which has been altered to define a polar grid for each lensing band in place of a Cartesian grid.

5   Results: Spectra for Sub-Keplerian Flow Disk Model

To examine the effects of varying the sub-Keplerianity factor ξ on the broadened iron emission lines, we kept the parameters $\beta_r = \beta_\phi = 1$ for the model of sub-Keplerian flow described in Section 4.2.3 and used $\xi = 0$, 0.25, 0.5, 0.75, 1 for each spin and observer inclination case. We chose the inner edge of the disk to be the ISCO radius and the outer edge of the disk to

be $r = 30M$, where the disk radius r has units of mass in natural units. For the image screen resolution, we used $d\rho = 0.005$ and $d\varphi = 0.0025$, where $d\rho$ represents the radial distance between points on the image screen with the newly defined polar grid and $d\varphi$ represents the angular distance between them. When we plot the histograms, binned by the observed energy, in the process of computing the broadened iron line with the method described in Section 3.4, we used a bin width of $dE = 0.025$, ten times that of the bin width used by Athena [26].

5.1 Low Spin, Low Inclination
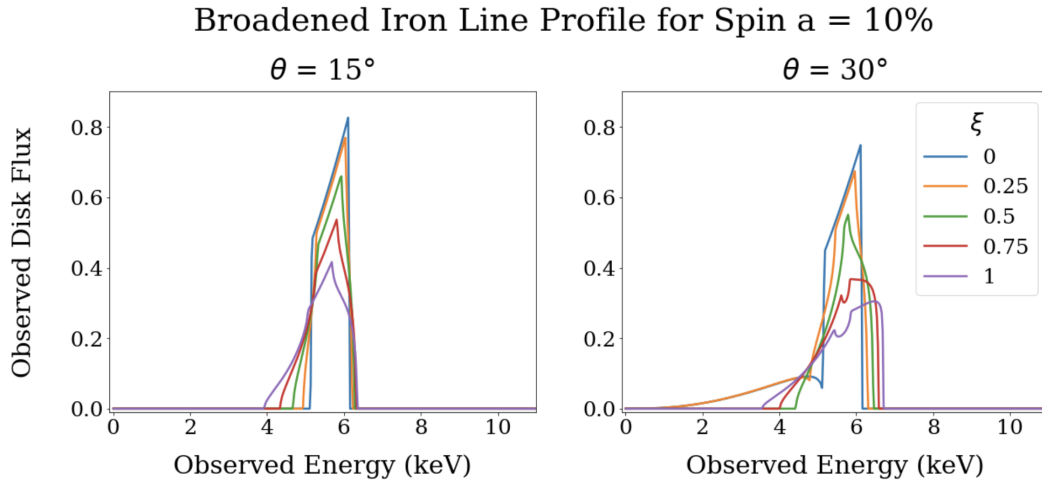
Figure 7: The broadened iron emission line spectra for different values of the sub-Keplerianity parameter ξ for spin $a = 10\%$ and observer inclination $\theta = 15°$ and $\theta = 30°$, constructed with the modified version of AART [19] described in Section 4.3.

Our simulated spectra indicate that for relatively low spin and low observer inclinations, the rightmost energy consistently increases as the sub-Keplerianity parameter ξ rises from 0 to 1. This increase is more pronounced with slightly higher observer inclinations, as illustrated in Figure 7. The energy at which the highest flux occurs decreases monotonically, except at an observer inclination of 30°, where it begins to increase at an increasing rate after $\xi = 0.5$. The leftmost energy, where the redshifted tails of the spectra truncate, generally decreases with increasing ξ. However, a distinct trend emerges when the observer inclination shifts from 15° to 30°. At $\theta = 30°$, the leftmost energy starts at $E_o = 0$ for $\xi = 0$ and $\xi = 0.25$ before experiencing a significant increase to about $E_o = 5$ keV at $\xi = 0.5$, followed by a subsequent decrease. The uniqueness of this trend makes it particularly interesting and worth exploring in detail in a future study.

5.2 Low Spin, High Inclination

For low spin and relatively high observer inclinations, the leftmost energy of the spectra decreases monotonically as ξ increases. Simultaneously, the rightmost energy appears to
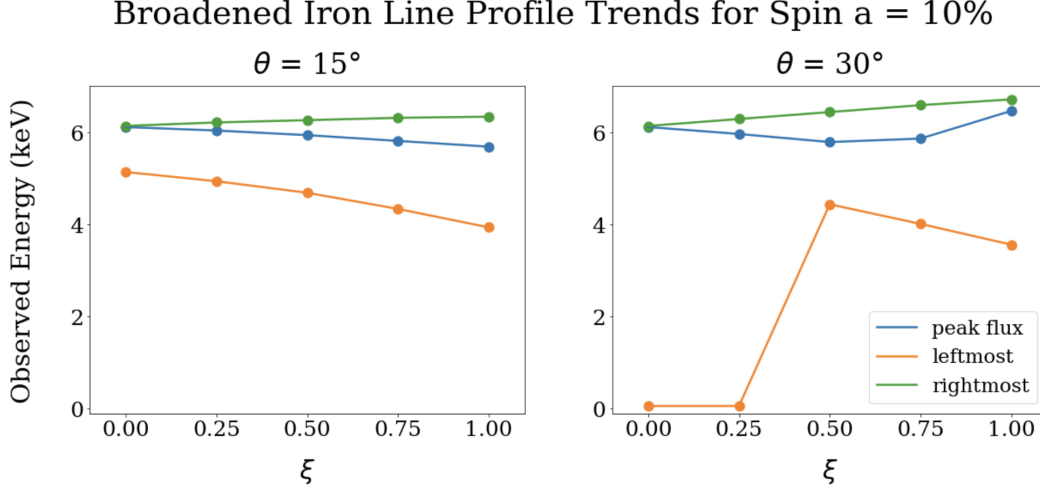
Figure 8: The leftmost energy, rightmost energy, and energy at which the highest flux occurs plotted with respect to ξ for the broadened iron emission line spectra for low spin and low inclination from Figure 7.
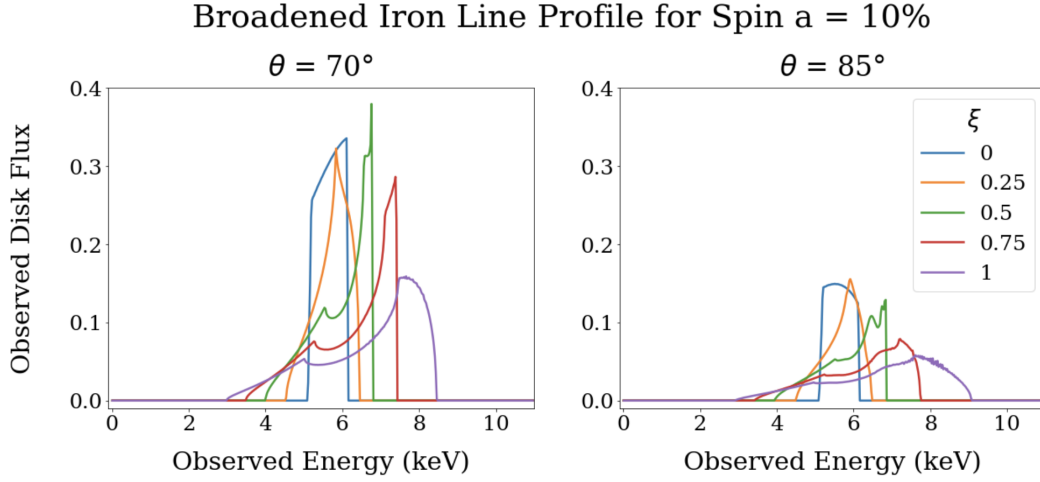

Figure 9: The broadened iron emission line spectra for different values of the sub-Keplerianity parameter ξ for spin $a = 10\%$ and observer inclination $\theta = 70°$ and $\theta = 85°$, constructed with the modified version of `AART` [19] described in Section 4.3.

increase monotonically for $0 < \xi < 0.5$ and at an increasing rate for $0.5 < \xi < 1$. The energy at which the highest flux occurs also generally increases, with a notable exception at $\theta = 70°$, where the peak flux energy decreases for $0 < \xi < 0.25$ and increases for $\xi > 0.25$. It can also be observed that for $\theta = 70°$ and $\xi = 0, 0.5, 0.75$, the peak flux energy is equal to the rightmost energy of the spectra. This can also be observed for $\theta = 85°$ and $\xi = 0.5$.
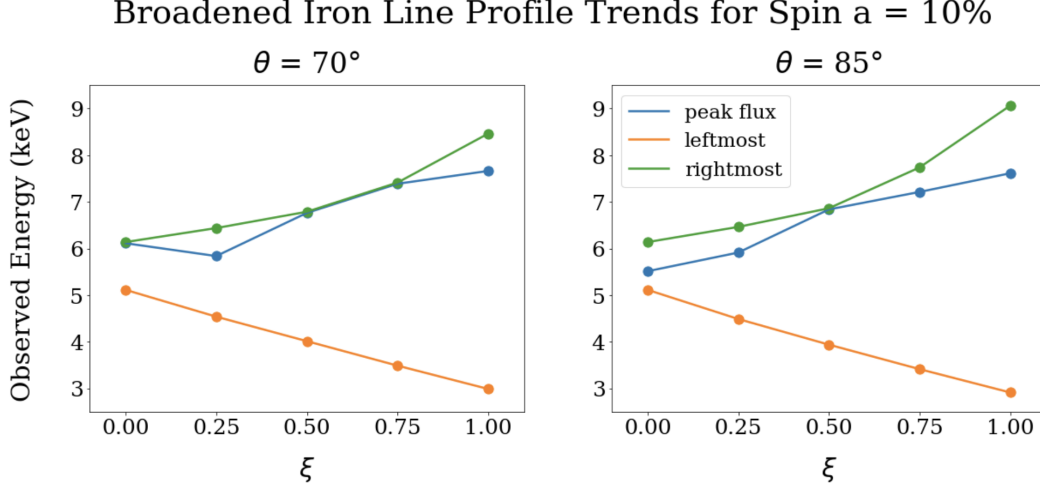
Figure 10: The leftmost energy, rightmost energy, and energy at which the highest flux occurs plotted with respect to ξ for the broadened iron emission line spectra for low spin and high inclination from Figure 9.
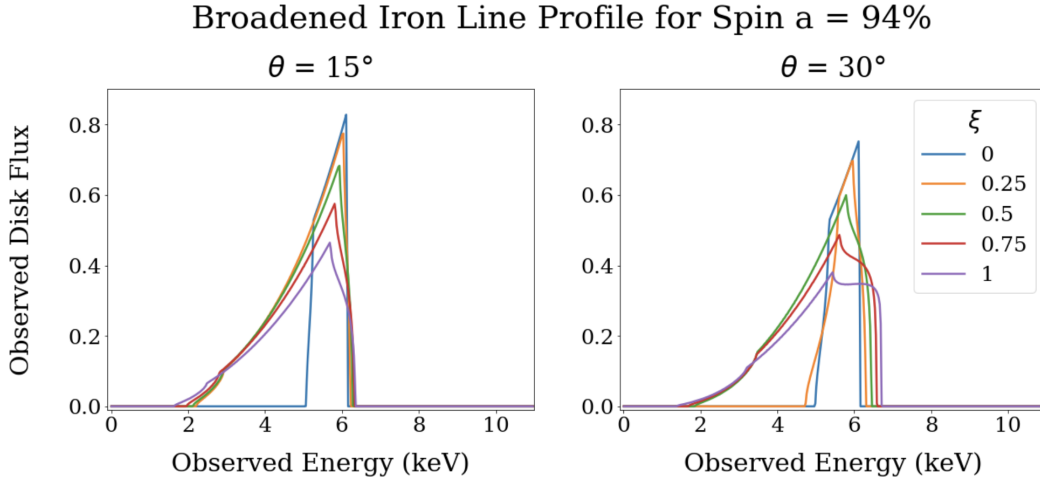
5.3 High Spin, Low Inclination

Figure 11: The broadened iron emission line spectra for different values of the sub-Keplerianity parameter ξ for spin $a = 94\%$ and observer inclination $\theta = 15°$ and $\theta = 30°$, constructed with the modified version of AART [19] described in Section 4.3.

For high spin and relatively low observer inclinations, the rightmost energy of the spectra increases monotonically as ξ increases, while the peak flux energy decreases monotonically. The leftmost energy of the spectra does not appear to follow a simple pattern as the peak flux and rightmost energies do. In both observer inclination cases for high spin, the leftmost energy begins at around $E_o = 5$ keV at $\xi = 0$ and ends at around $E_o = 1.5$ keV at $\xi = 1$.
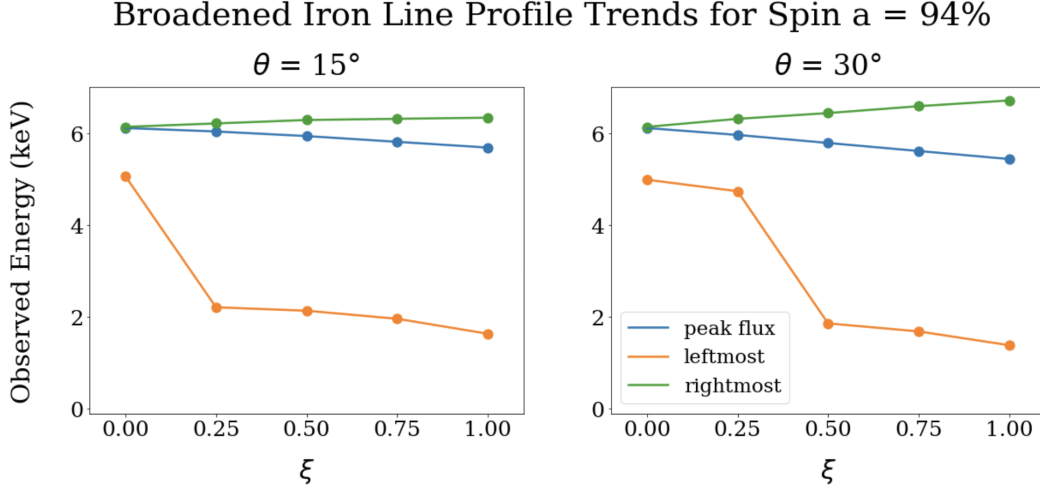
Figure 12: The leftmost energy, rightmost energy, and energy at which the highest flux occurs plotted with respect to ξ for the broadened iron emission line spectra for high spin and low inclination from Figure 11.

There is a large jump in the leftmost energy as ξ increases. Specifically, for $\theta = 15°$, there is a significant decrease in the leftmost energy from $\xi = 0$ to $\xi = 0.25$, and for $\theta = 30°$, there is one from $\xi = 0.25$ to $\xi = 0.5$, both of which can be seen in Figure 12. This irregularity in the trend of the leftmost energy with respect to ξ presents another anomaly worth exploring.

5.4 High Spin, High Inclination

The spectra for high spin and relatively high observer inclinations demonstrate the most consistently observed trends among all the spectra analyzed in the previous three subsections. The leftmost energy of the iron line exhibits only a slight decrease from $\xi = 0$ to $\xi = 1$ for both observer inclinations, creating minimal differences in the leftmost energy between the lines for different ξ values. Additionally, we observe both the rightmost and peak flux energies increasing as ξ increases and notice that for $\theta = 70°$ and $\xi = 0.5, 0.75, 1$, the peak flux energy is equivalent to the rightmost energy.

6 Conclusion

In this paper, we modeled the broadened iron emission line spectra of BH accretion disks produced by the X-ray reflection method for the disk model of sub-Keplerian flow, where the angular momentum from the standard model of stable circular orbits are rescaled by a sub-Keplerianity parameter ξ (Section 4.2.3). To create the spectra, we used AART, an adaptive analytical ray-tracing code from Cárdenas-Avendaño et al. designed to simulate high-resolution images of BH accretion disks and calculate the disk radii r and redshift factors g at each pixel in the image [19]. The models we produced for various sub-Keplerianity
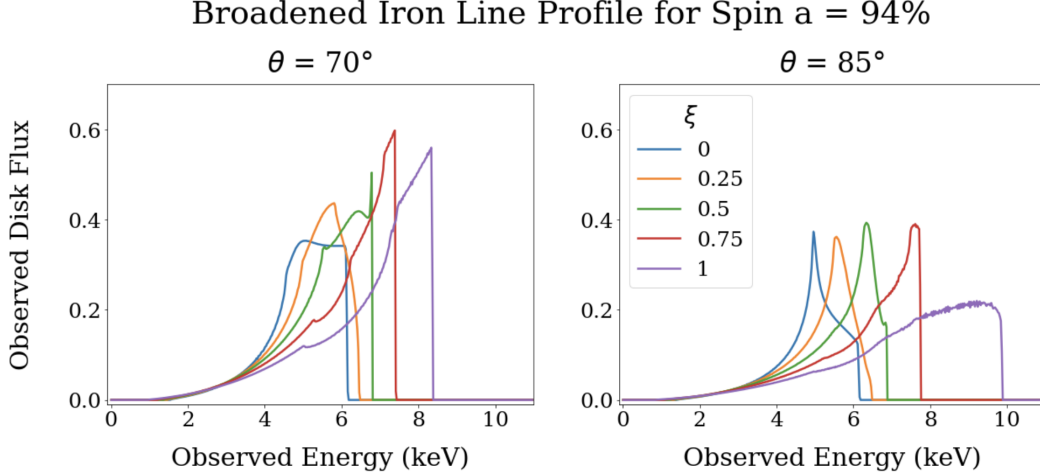
Figure 13: The broadened iron emission line spectra for different values of the sub-Keplerianity parameter ξ for spin $a = 94\%$ and observer inclination $\theta = 70°$ and $\theta = 85°$, constructed with the modified version of `AART` [19] described in Section 4.3. For both observer inclinations, we notice noise near the peak of the line profiles for $\xi = 0.75$ and $\xi = 1$.
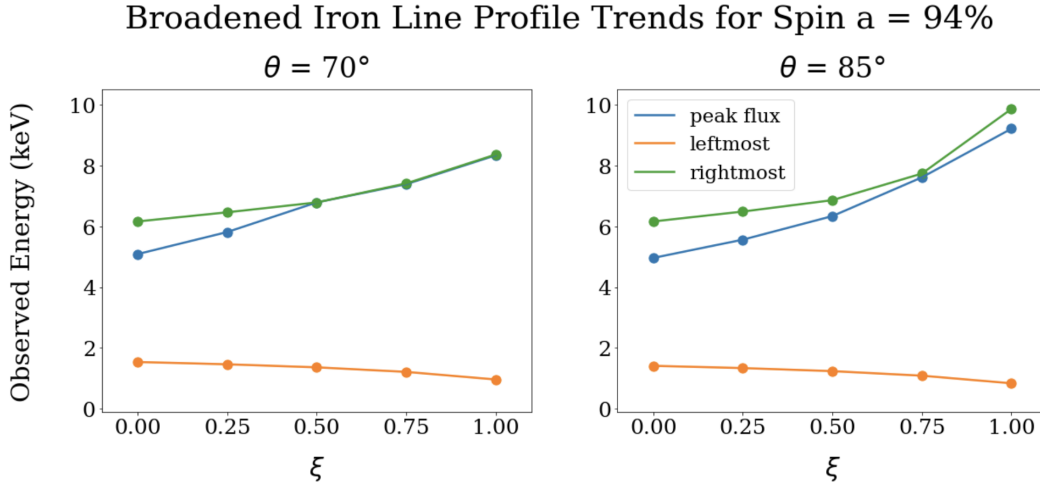

Figure 14: The leftmost energy, rightmost energy, and energy at which the highest flux occurs plotted with respect to ξ for the broadened iron emission line spectra for high spin and high inclination from Figure 13.

parameter values with different spin and observer inclination cases can be seen in Figures 7, 9, 11, and 13.

Some limitations to our work include our assumption of the Novikov-Thorne model, which describes a geometrically thin, optically thick accretion disk [17]. With this model, we assume all light rays crossing the disk equatorial plane are absorbed. Another limitation is our fixed disk inner edge at $r = r_{ISCO}$ and fixed outer edge at $r = 30M$. For future studies, we can explore models of accretion disk flow within ISCO radius and the effects

of increasing the maximum disk radius. It would also be worthwhile to explore models of spectra of optically thin disks and the effects of considering the lensed emissions from the disk for $n > 0$. Furthermore, for some of the simulated iron line emission spectra, we notice noise, in Figure 13 for example. Thus, we must also continue to perform convergence tests to determine which image screen resolution ($d\rho$, $d\varphi$) is needed for Modified-`AART` (Section 4.3) to simulate spectra at a resolution level akin to that from the proposed Athena observatory mission [26].

The work done in this paper lays the groundwork for future simulations of iron line spectra using non-standard accretion disk models. Potentially worthwhile future efforts include running simulations with higher resolutions perform more detailed scans across the line profiles, focusing on the leftmost, rightmost, and peak flux energies.

References

[1] K. Gebhardt et al., *THE BLACK HOLE MASS IN M87 FROM GEMINI/NIFS ADAPTIVE OPTICS OBSERVATIONS*, ApJ **729** (2011).

[2] A. M. Ghez et al., *Measuring Distance and Properties of the Milky Way's Central Supermassive Black Hole with Stellar Orbits*, ApJ **689** (2008).

[3] T. E. H. T. C. et al., *First M87 Event Horizon Telescope Results. VI. The Shadow and Mass of the Central Black Hole*, ApJ **875** (2019).

[4] T. E. H. T. C. et al., *First Sagittarius A* Event Horizon Telescope Results. IV. Variability, Morphology, and Black Hole Mass*, ApJ **930** (2022).

[5] I. M. George and A. C. Fabian, *X-ray reflection from cold matter in Active Galactic Nuclei and X-ray binaries*, Monthly Notices of the Royal Astronomical Society **249**, 352 (1991).

[6] L. W. Brenneman and C. S. Reynolds, *Constraining Black Hole Spin via X-Ray Spectroscopy*, ApJ **652**, 1028 (2006).

[7] C. S. Reynolds, *Observing black holes spin*, Nature Astronomy **3** (2019).

[8] C. S. Reynolds, *Observational Constraints on Black Hole Spin*, Annual Review of Astronomy and Astrophysics **59**, 117 (2020).

[9] D. E. A. Gates, S. Hadar, and A. Lupsasca, *Maximum Observable Blueshift from Circular Equatorial Kerr Orbiters*, Phys. Rev. D **102**, 104041 (2020).

[10] C. T. Cunningham, *The effects of redshifts and focusing on the spectrum of an accretion disk around a Kerr black hole*, ApJ **202**, 788 (1975).

[11] J. García and T. R. Kallman, *X-ray Reflected Spectra from Accretion Disk Models. I. Constant Density Atmospheres*, ApJ **718**, 695 (2010).

[12] `xillver` Documenation.

[13] T. Dauser, J. Wilms, C. S. Reynolds, and L. Brenneman, *Broad emission lines for a negatively spinning black hole*, Monthly Notices of the Royal Astronomical Society **409**, 1534 (2010).

[14] `relline` Documenation.

[15] J. García *et al.*, *Improved Reflection Models of Black Hole Accretion Disks: Treating the Angular Distribution of X-Rays*, ApJ **782**, 76 (2014).

[16] `relxill` Documenation.

[17] I. D. Novikov and K. S. Thorne, *Astrophysics of black holes*, p. 343 (1973).

[18] R. H. Boyer and R. W. Lindquist, *Maximal Analytic Extension of the Kerr Metric*, J. Math. Phys. **8** (1967).

[19] A. Cárdenas-Avendaño, A. Lupsasca, and H. Zhu, *Adaptive Analytical Ray Tracing of Black Hole Photon Rings*, Phys. Rev. D **107**, 043030 (2023).

[20] S. E. Gralla and A. Lupsasca, *Lensing by Kerr Black Holes*, Phys. Rev. D **101** (2020).

[21] J. P. Luminet, *Image of a spherical black hole with thin accretion disk*, Astronomy and Astrophysics **75**, 228 (1979).

[22] AART Documentation.

[23] J. M. Bardeen, W. H. Press, and S. A. Teukolsky, *Rotating Black Holes: Locally Non-rotating Frames, Energy Extraction, and Scalar Synchrotron Radiation*, ApJ **178**, 347 (1972).

[24] F. H. Vincent, S. E. Gralla, A. Lupsasca, and M. Wielgus, *Images and photon ring signatures of thick disks around black holes*, Astronomy and Astrophysics **667** (2022).

[25] H.-Y. Pu, K. Akiyama, and K. Asada, *THE EFFECTS OF ACCRETION FLOW DY-NAMICS ON THE BLACK HOLE SHADOW OF SAGITTARIUS A**, ApJ **831** (2016).

[26] D. Barret et al., *The Athena X-ray Integral Field Unit (X-IFU)*, Space Telescopes and Instrumentation 2016: Ultraviolet to Gamma Ray **9905** (2016).